Chapter 4

Nanoscale Mechanical Properties of LB Films of PyTp and PyTp - DNA Complex by Atomic Force Microscopy

4.1 Introduction

In the previous chapter, we have shown the formation of stable complex between a cationic discotic mesogen, viz., pyridinium tethered with hexaalkoxytriphenylene (PyTp), and DNA. The most interesting feature was that the PyTp-DNA complex monolayer, which was formed at the air-water (A-W) interface, could be transferred successfully onto solid substrates. Mutlilayers containing as many as 50 layers could be formed on silicon substrates by LB technique with transfer efficiency close to 100 %.

The discogen molecules are renowned for their intriguing supramolecular architechture. This makes them potential candidate for various applications (discussed in Chapter 1). The DNA molecule, containing the genetic code of all living species, has also caught lot of attention due to its potential application in nanoelectronic devices. Therefore, a combination of cationic discogen and DNA is an unique approach towards the development of advanced materials with novel electrical and mechanical properties. In literature, there are several reports on the studies of aliphatic cationic lipid-DNA complexes, which are primarily stimulated by nonviral gene delivery [1, 2]. There are also efforts for using such lipid-DNA complexes for organic electronics [3], biosensors [4], biomedical applications [5] and optical applications [6]. Although aliphatic lipid-DNA complexes are known for decades, the discogen-DNA complex is being studied recently [7, 8] and

they are expected to have some novel applications. For any practical application, well ordered thin film is a necessity. Although there are several techniques to obtain thin films, LB technique is a convenient approach to obtain well ordered films under controlled conditions [9].

The successful long-term performance and reliability of these materials in practical devices are usually limited by their mechanical properties. Hence, measurements of the mechanical properties of such materials are of paramount importance. These properties may vary significantly depending on the length scale. Particularly, the properties exhibited by a material at the nanoscale may differ from those exhibited at the macro scale. The conventional techniques to measure the mechanical properties of materials are generally restricted to macroscopic length scale, whereas the current trend in miniaturization of products and devices pose the need for characterization of materials at the nanoscale. Therefore, it has become necessary to implement nanoscale property measurement techniques. One of the convenient and reliable methods for the precise measurement of mechanical properties of nanostructures is to employ an atomic force microscope (AFM). An AFM can provide direct spatial mapping of surface topography, heterogeneity, and elasticity with nanoscale resolution [10]. Compared with other tools, AFM can probe local surface elastic properties of soft systems quantitatively by indentation method with precise control of applied force, down to few nanoNewtons [11, 12]. In addition, the phase shift measurements in tapping mode AFM can be used to qualitatively characterize the material surface properties, such as stiffness and viscoelasticity [13]. In tapping mode AFM, the tip intermittently touches the surface, minimizing the destructive lateral forces; thereby making it suitable for the study of soft biological systems and also for systems where the molecules are weakly adsorbed to the substrate (e.g., LB films). The combination of nanoindentation and phase shift measurements with AFM is an useful approach for studying the mechanical properties of film surfaces at the nanoscale [14].

In this chapter, we present our studies on the mechanical properties of the LB films of PyTp as well as PyTp-DNA complex using an AFM. To measure the local elasticity of these films, nanoscale indentation was performed in the contact mode AFM and force-distance curves were obtained. It is a common practice to use the Hertz contact mechanics model to describe the indentation of a non-deformable indenter into a deformable elastic surface [15]. We have used this model

for quantitative analysis of the force-distance curves obtained in the indentation measurements. In addition, both the PyTp and PyTp-DNA complex films were scanned in the tapping mode AFM and simultaneous topography and phase images were acquired. The phase images were used to construct the energy dissipation maps for qualitative characterization of stiffness variation in the films.

4.2 Experiment

The monolayer film of PyTp was prepared at the air-water (A-W) interface in a Langmuir trough. The PyTp-DNA complex monolayer film was prepared at the A-W interface with 10^{-8} M concentration of DNA in the ultrapure water subphase. The details of film formation are presented in Chapter 2 and Chapter 3. These films were transferred at a target surface pressure of 35 mN/m onto polished silicon substrates by LB technique. We have shown in the previous chapters that, at this surface pressure, the PyTp molecules in the monolayer exhibit an edge-on configuration. We have carried out nanoindentation and phase shift measurements on these LB films using a multimode AFM. For nanoindentation studies, we have used LB films with 2 layers and for phase shift measurements, we have used LB films with 1, 2, 5 and 20 layers. All the films with odd number of layers were transferred on hydrophilic silicon substrates, and those with even number of layers were transferred on hydrophobic silicon substrates. All the measurements were carried out at room temperature ($\sim 25\ ^0$C).

To measure the elastic properties of the films, AFM was used in the contact mode to perform nanoindentation. Instead of scanning with the tip laterally across the sample surface, the tip was positioned above the surface and moved vertically down. The cantilever deflection, as measured with the optical lever detection system, was plotted as a function of the vertical motion of the piezoelectric scanner to produce a force-distance curve. The advantage of using AFM as a nanoindenter is that we can have fine control on the applied load, down to fraction of nanoNewton. In addition, it was possible to observe the deformation (elastic or plastic) by imaging the area before and after indentation. In the previous chapter, we presented the indentation measurements performed under plastic deformation and determined the hardness of the films. In the work described in the present

chapter, we have kept the depth of indentation to be small to avoid any plastic deformation. Under this condition, we have measured the elastic modulus of the films.

The measurements were carried out inside an environmental chamber in which dry nitrogen gas was circulated to avoid capillary condensation of water at the contact point between the tip and the surface. Freshly cleaned silicon wafer was used as a hard non-deformable reference substrate for photodetector sensitivity calibration. V-shaped silicon nitride cantilevers with a tip radius of 15 nm (Nanosensors) were used. The spring constant of the cantilevers were in the range of 0.06 to 0.10 N/m, as determined by measuring the free resonance frequency in air using ThermalK software (Molecular Imaging). To determine the spring constant, the cantilever was taken away from the sample (i.e., no tip-sample interaction) and its thermal fluctuations were measured. The cantilever was driven by an AC signal to obtain its resonance frequency. A power spectrum of the AC signal yielded the mean-square amplitude of the cantilever oscillation, which was then used to evaluate the spring constant using the ThermalK software.

In addition, the topography and phase images of the films were obtained simultaneously using tapping mode AFM (TM-AFM). Here, the cantilever oscillates close to its resonance frequency and the tip makes contact with the sample surface only for a short duration ($\sim 10^{-7}$ seconds) in each oscillation cycle. As the tip approaches the sample, the amplitude and phase angle of the oscillating cantilever change due to the tip-sample interaction. The change in the phase angle produces the phase image which can provide significantly more contrast than the topography image. We have used super sharp probes made up of single-beam silicon cantilevers with a spring constant of 47 N/m and a tip radius typically of 2 nm. The cantilever was oscillated at a frequency of about 200 Hz below its resonance frequency (~163 kHz) with a free amplitude in the range of 40 to 55 nm. The images were acquired at a scan rate of 2 Hz. To represent phase shifts, we have adopted the standard convention that assigns a 90^0 phase shift lag between the excitation and response when the free cantilever is excited at its fundamental resonance [16]. Driving frequencies below the free resonance would produce phase shifts between 0^0 and 90^0 yielding a repulsive interaction regime, while frequencies above resonance would produce phase shifts between 90^0 and 180^0 yielding an attractive interaction regime. In all our measurements, the driving frequencies were below the free

resonance producing phase shifts between 0^0 and 90^0 in the repulsive interaction regime.

4.3 Theory

4.3.1 Determination of Young's elastic modulus

To determine Young's elastic modulus, we have carried out nanoindentation measurements using an AFM in the contact mode. Here, we obtain cantilever deflection (d) versus piezo displacement (z) curves. These curves can be converted into force (F) versus indentation depth (δ) curves using Hooke's law,

$$F = k_c\, d \tag{4.1}$$

where k_c is the spring constant of the cantilever. The indentation depth δ is given by,

$$\delta = z - d \tag{4.2}$$

For a precise measurement of the applied force, it is important to determine the k_c accurately. (The k_c values provided by manufacturer may suffer from an error bar as high as 50 %.) Although there are several methods to determine the k_c of a cantilever [17], the thermal method is widely preferred. This method is easy to use and is independent of cantilever's geometry and material [18]. This is based on a fundamental physics theorem, i.e., the theorem of equipartition, which states that the average value of each quadratic term in the Hamiltonian of a system is given by $k_BT/2$, where k_B is Boltzmann's constant and T is the temperature. Here, a cantilever can be treated as a harmonic oscillator in equilibrium with its surroundings which fluctuates in response to thermal noise. The Hamiltonian of such a system is given by

$$H = \frac{p^2}{2m} + \frac{m\omega_o^2 q^2}{2} \tag{4.3}$$

where q is the fluctuation of the oscillator (cantilever), p is its momentum, m is the oscillating mass, and ω_o is the resonant angular frequency of the system. By equipartition, one can write,

$$\left\langle \frac{m\omega_o^2 q^2}{2} \right\rangle = \frac{k_B T}{2} \tag{4.4}$$

Since $\omega_o^2 = k_c/m$, the spring constant k_c can be obtained from the above equation by measuring the mean-square amplitude ($< q^2 >$) of cantilever oscillation as

$$k_c = \frac{k_B T}{< q^2 >} \tag{4.5}$$

For a k_c of 0.05 N/m, which is a typical value for relatively weak cantilevers, the thermal fluctuations will be of the order of 3 Å at room temperature. For such small deflections, we can approximate an AFM cantilever as a simple harmonic oscillator with one degree of freedom. The mean-square amplitude of the oscillation can be obtained from the integral of the power spectra of AC signal which is used to drive the cantilever.

From the F versus δ curves, it is possible to draw information about the elasto-plastic behavior of materials [15]. For an ideally elastic sample (Figure 4.1(a)), when the tip approaches, i.e., from O to A, it penetrates the sample upto a depth δ, causing a deformation. During the withdrawal, the tip goes back from A to O, and since the sample is elastic, it recovers step by step its own shape, exerting the same force on the tip. Hence, loading and unloading curves, i.e., the approach and withdrawal lines, overlap. If the sample is ideally plastic (Figure 4.1(b)), it undergoes a deformation during the loading curve. When the tip is withdrawn, the sample does not recover its own shape and the load decreases, whereas the indentation depth stays the same. Most of the samples have a mixed behavior. Hence, loading and unloading curves seldom overlap. In particular, at a given penetration depth, the force of the unloading curve is lesser than the force of the loading curve (Figure 4.1(c)). The difference between the approach and the withdrawal lines is called "loading-unloading hysteresis". The indentation depth H$'$ at which the force of the unloading curve equals zero is called "zero load plastic deformation". The indentation depth H upto which the sample recovers is called the "zero load elastic deformation".

In the following, we neglect the plastic deformations and review the models dealing with elastic continuum contact mechanics, in which the tip and the sample are assumed to be continuous

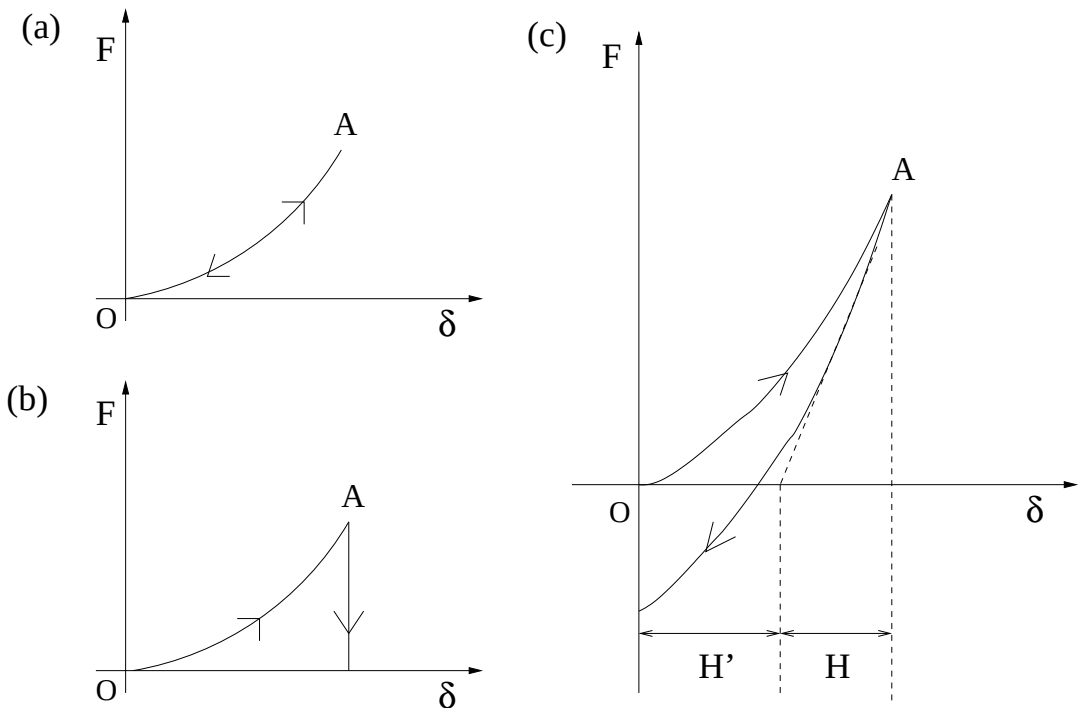

Figure 4.1: Force (F) versus indentation (δ) curves for (a) an ideally elastic material, (b) an ideally plastic material, and (c) an elasto-plastic material. H$'$ is the 'zero load plastic deformation', i.e., the indentation depth at which the force of the unloading curve equals zero. H is the 'zero load elastic deformation', i.e., the indentation depth upto which the sample recovers.

elastic media. The basic model which describes the elastic deformation of two surfaces touching under load was developed by Hertz in 1881 [19]. Hertz model is commonly used to describe the indentation of a non-deformable indenter (the AFM tip) into an infinitely extending deformable elastic half space (the sample surface), subject to a number of important assumptions [20]. The principal assumptions are: (i) a normal load exists at the contact between the tip and the sample, (ii) the radius of contact area is small compared with the radius of the tip, and (iii) there is no adhesion and friction between the tip and sample.

The AFM tip shape can be generally modeled by two geometries; a conical indenter and a paraboloid or spherical indenter. For these two cases, the Hertz model predicts a different functional relationship between the loading force needed to create an indentation. In the case of a conical tip indenting a soft sample, the relationship between the loading force (F) and resulting indentation (δ) is given by the following expression:

$$F_{cone} = \frac{2}{\pi} tan\,\alpha\, E^* \delta^2 \tag{4.6}$$

In the case of a paraboloid or spherical tip indenting a soft sample, the Hertz model gives the following relation between the F and δ:

$$F_{paraboloid} = \frac{4}{3} E^* R^{1/2} \delta^{3/2} \tag{4.7}$$

In these relations, α is the half-opening angle of a conical tip, R is the radius of curvature of a spherical or paraboloid indenter. E^* is the reduced elastic modulus of tip-sample system and is defined by the following equation

$$\frac{1}{E^*} = \frac{1-\nu^2}{E} + \frac{1-{\nu_1}^2}{E_1} \tag{4.8}$$

where E and E_1 are the elastic modulus, and ν and ν_1 are the Poisson's ratios, of the sample and the tip, respectively. (When a material is stretched in one direction, it contracts in a direction at right angles to the direction of stretching. The ratio of this transverse contraction in dimension to that of the extension in the direction of stretching is the Poisson's ratio of the material [21]. It is usually a positive number less than 0.5.) The AFM tip made up of silicon has a bulk elastic modulus [20] of 130-160 GPa and $\nu_1 = 0.27$. Assuming $E \ll E_1$, we can approximate the above equation as

$$E^* \approx \frac{E}{1-\nu^2} \tag{4.9}$$

where E is the Young's elastic modulus of the sample and ν is its Poisson's ratio [22]. From expressions 4.6 and 4.7, one can see that if a quadratic relation is observed between F and δ, a conical model should be used for the tip, while if the F versus δ relation is close to a $\delta^{3/2}$ variation, the spherical or paraboloid model should be used.

The Hertz model can successfully describe the F versus δ curves whenever the surface forces (e.g., adhesion) are negligible. This model needs correction, for the cases where the surface forces

can not be neglected. Two models, Derjaguin-Muller-Toporov (DMT) and Johnson-Kendall-Roberts (JKR), have been widely adopted to correct for the behavior of Hertzian contacts in presence of surface forces. The DMT model is applicable for systems with low adhesion and small tip radii, whereas the JKR model is suitable for highly adhesive with low stiffness and large tip radii. In all the indentation measurements , we have used the Hertz model since the adhesion was negligible in our system. However, the detailed description of DMT and JKR models can be found in a report by Cappella and Dietler [15].

4.3.2 Determination of Energy Dissipation

The energy dissipation was determined by measuring the phase shift using an AFM in the tapping mode. Here, the cantilever is oscillated at a frequency close to its resonance. The cantilever oscillation is driven by an external and sinusoidal signal. The dominant contributions considered in the equation of motion of the cantilever are: (i) elastic response, (ii) hydrodynamic damping with the medium, (iii) tip-sample interaction, and (iv) excitation force. The resulting second-order differential equation is as follows [23]:

$$m\frac{d^2z}{dt^2} = -k_c z - \frac{m\omega_0}{Q}\frac{dz}{dt} + F_{ts} + F_0 cos\,\omega t, \tag{4.10}$$

where F_0 and ω ($\omega = 2\pi f$) are the amplitude and angular frequency of the driving force, respectively. Q, ω_0 and k_c are the quality factor, angular resonance frequency and spring constant of the free cantilever, respectively. ω_0 is related to k_c and m by the relation $k_c = m\omega_0^2$. F_{ts} denotes the tip-sample interaction. The above equation implies several assumptions. (i) It considers the cantilever as a point mass spring. (This assumption ignores the contribution of the higher flexural modes of the cantilever motion [24].) (ii) The Q-factor used here is independent of tip-sample separation. (This assumption neglects changes in the hydrodynamic damping of the cantilever during its motion [25].) From this equation, we can derive expressions for the phase angle of a freely oscillating (i.e., no tip-sample interaction) cantilever as well as the phase angle for an interacting cantilever.

For a freely oscillating cantilever, the phase angle (in radians) is expressed as:

$$\phi_{free} = tan^{-1}\left(\frac{m\omega\omega_0}{Q(k_c - m\omega^2)}\right) \tag{4.11}$$

The angle ϕ_{free} varies sharply around ω_0 as a function of ω. ϕ_{free} is $\pi/2$ at $\omega = \omega_0$, smaller than $\pi/2$ at $\omega < \omega_0$, and greater than $\pi/2$ at $\omega > \omega_0$. When an oscillating cantilever is brought close to a sample surface, the amplitude of oscillation and its frequency change due to the tip-sample interactions. As a consequence, the spring constant of the cantilever changes to a new effective value $k_{eff} = k_c + \sigma$, where σ represents the sum of the force derivatives for all the forces F_{ts} acting on the cantilever;

$$\sigma = \Sigma \frac{\partial F_{ts}}{\partial z} \tag{4.12}$$

Here, z is the distance between the tip and sample. The phase angle of the interacting cantilever can be expressed as

$$\phi_{int} = tan^{-1}\left(\frac{m\omega\omega_0}{Q(k_c + \sigma - m\omega^2)}\right) \tag{4.13}$$

provided that σ is very small in magnitude compared with k_c. From this expression, the phase angle at $\omega = \omega_0$ of the interacting cantilever is given by

$$\phi_{int} = tan^{-1}\left(\frac{k_c}{Q\sigma}\right) \tag{4.14}$$

Therefore, the phase angle shift $\Delta\phi_0$ between the free and the interacting cantilevers at $\omega = \omega_0$ is given by,

$$\Delta\phi_0 = \phi_{free} - \phi_{int} = \frac{\pi}{2} - tan^{-1}\left(\frac{k_c}{Q\sigma}\right) \approx \frac{Q\sigma}{k_c} \tag{4.15}$$

where the approximate relationship holds when σ is very small in magnitude compared with k_c. It should be noted that the sign of the phase angle shift $\Delta\phi_0$ coincides with that of the overall force derivative σ. Thus, $\Delta\phi_0$ (hereafter referred to as phase shift and denoted by ϕ) is positive when the overall force acting on the tip is repulsive and negative when the overall force is attractive.

In tapping mode AFM, the elastic deformation of a sample surface associated with the tip-sample repulsive force can be estimated by the Hertz model (section 4.3.1). Considering a spherical tip under force F on a plane surface, the surface stiffness S is expressed as:

$$S = \frac{\partial F}{\partial \delta} = \epsilon\, a\, E^*; \tag{4.16}$$

where a is the radius of the circular contact area, δ is the indentation depth, E^* is the reduced elastic modulus of the tip-sample system and ϵ is a constant [26]. When the tip and sample come into contact and their repulsive force indents the surface, it is reasonable to approximate the overall force derivative σ by the stiffness of the tip and the sample. The stiffness defined by the above equation is valid when the tip is in contact with a sample surface. In tapping mode, the tip makes only a momentary contact ($\sim 10^{-7}$ seconds) in each cycle of oscillation, and the tip-sample contact area varies with time throughout the duration of each contact. For the qualitative discussion of phase angles, therefore, it is appropriate to use the time-averaged values of the contact radius a ($< a >$) and stiffness S ($< S >$) over one cycle of oscillation. When the overall force derivative σ is dominated by the surface stiffness ($\sigma \approx < S > = \epsilon < a > E^*$), the equation 4.15 becomes

$$\phi \approx < S > \left(\frac{Q}{k_c}\right) = \epsilon\ < a >\ E^* \left(\frac{Q}{k_c}\right) \tag{4.17}$$

Equation 4.17 shows that the phase imaging provides a map of stiffness variation on the sample surface such that a stiffer region has a more positive phase shift and hence appears brighter in a phase image. In general, a softer material leads to a larger contact area $< A >$, and the duration of the tip-sample contact is longer on a softer material than on a harder material. Consequently,

$< S >$ can be dominated by the contact area $< A >$ rather than E^* (i.e. $< S > \propto < a > \propto \sqrt{< A >}$), which makes the phase shift greater on a softer material than on a harder material [26].

However, these phase shift measurements depend more on the interaction regime than on the tip-sample interactions [27]. This makes the direct phase shift measurements less sensitive to the material properties. Martinez et al. have demonstrated that by converting phase shifts into energy dissipation data, the material properties become more sensitive to the tip-sample interactions [16], thereby giving the stiffness variation of the surface. A relationship between the phase shift and the energy dissipation can be obtained [28] by considering that in the steady state

$$E_{ext} = E_{air} + E_{dis}. \tag{4.18}$$

Here, E_{ext} is the external energy supplied to the cantilever, E_{air} is the energy dissipated via hydrodynamic viscous interactions with the environment, and E_{dis} is the energy dissipated due to the tip-sample interaction. From this equation, the following expression was proposed by Tamayo and Garcia [29] that relates the phase shift angle (ϕ) to the E_{dis} per cycle.

$$E_{dis} = \frac{\pi k_c A_0 A_{sp}}{Q}\left(sin\phi - \frac{f A_{sp}}{f_0 A_0}\right) \tag{4.19}$$

Here, f and f_0 are the excitation (driving) and natural (resonance) frequencies of the cantilever respectively. A_{sp} and A_0 are the set point (tapping) and the free oscillation amplitudes respectively. Q is the quality factor of the cantilever. Thus, the phase shift measurements can be conveniently transformed into energy dissipation values by means of equation 4.19. Then these measurements can be used to map variations in material properties like stiffness.

4.4 Results

4.4.1 Young's Elastic Modulus by Nanoindentation using AFM in the Contact Mode

Quantitative measurements of local elasticity was performed on LB films with two layers for both PyTp and PyTp-DNA complex. The cantilever deflection (d) versus piezo displacement (z) curves were obtained at several regions on these films and were converted into load (F) versus indentation (δ) curves using equations 4.1 and 4.2. Figure 4.2(a) shows the plot of d as a function of z obtained on a hard reference silicon surface and PyTp film surface with two layers. Figure 4.2(b) shows the plot obtained similarly for the PyTp-DNA complex film with two layers. For hard reference silicon surface, the slope of the d versus z curve was equal to 1, whereas for the film surfaces, the slope was less than 1. The difference between the cantilever deflection for the hard silicon surface and that for the soft film surface gives the indentation depth δ of the tip into the sample surface. Typical F versus δ curves obtained for the pure and complex films are shown in Figures 4.3(a) and 4.3(b) respectively. It was observed that for a given load, the depth of indentation was more on the pure film than on the complex film. For example, at a load of 0.2 nN, the indentation depth was 0.6 nm for the pure film and 0.3 nm for the complex film.

In addition, the F versus δ curves were analyzed quantitatively with Hertz model from continuum mechanics of contact to extract the values of Young's elastic modulus. We find that our measured F versus δ curves followed a $\delta^{3/2}$ variation for both the pure and complex film surfaces. Therefore, the curves were fitted using the paraboloid model (equation 4.7) and E^* values were extracted. More than 30 such curves were obtained at different positions on the film surfaces with different applied loads. The solid lines in Figures 4.3(a) and 4.3(b) represent the fitting of typical F versus δ curves with the paraboloid model to extract E^* values. We find that, for both the pure and complex films, the correlation between the data and the fit was better than 98%. Figures 4.4(a) and 4.4(b) show the E^* values obtained at different positions on the films with different loads . From these plots, the average E^* values obtained were 71.6 ± 3.2 MPa and 212.4 ± 3.0 MPa for the pure and complex films respectively. Using these E^* values and assuming a Poisson's ratio of 0.5 (which is expected for soft materials [12]) in equation 4.9, we have calculated the Young's

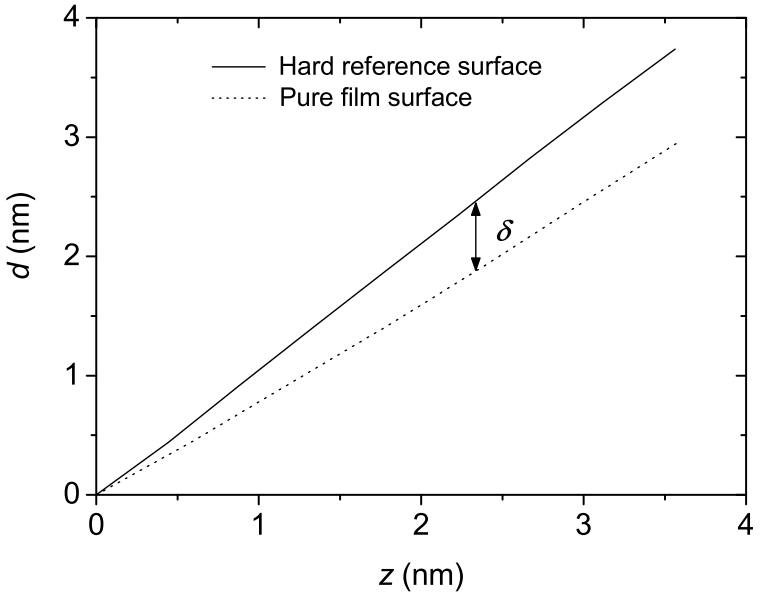

(a)

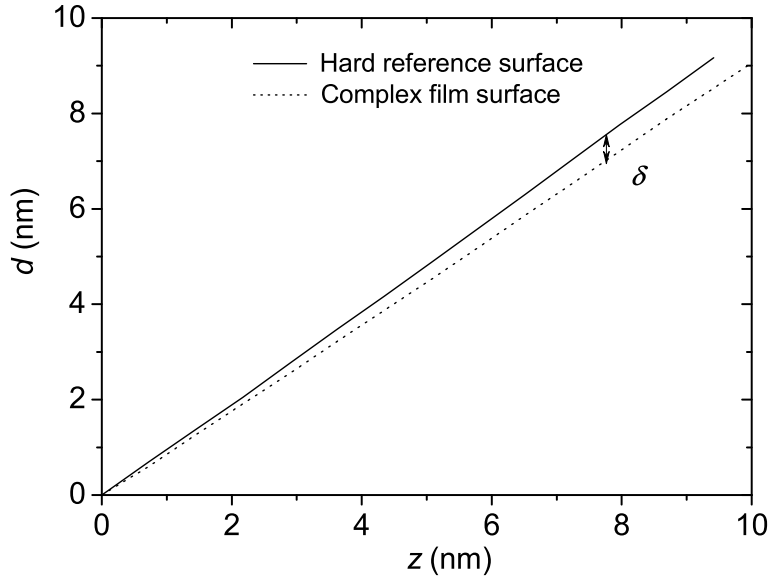

(b)

Figure 4.2: Cantilever deflection d versus piezo displacement z curves measured on LB films with two layers of (a) PyTp film, and (b) PyTp-DNA complex film. The solid lines represent the d versus z curves obtained on a hard reference silicon surface and the dotted lines represent the curves obtained on the film surfaces. The difference δ between the curves is equal to the tip indentation depth.

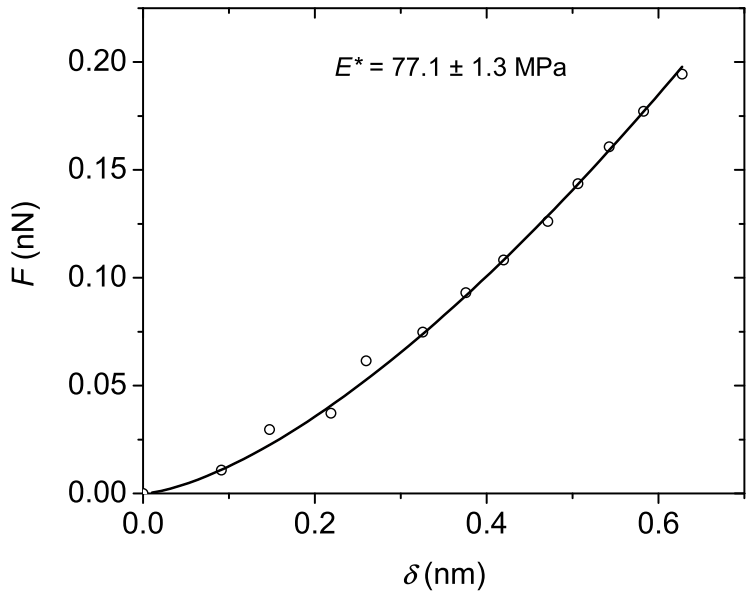

(a)

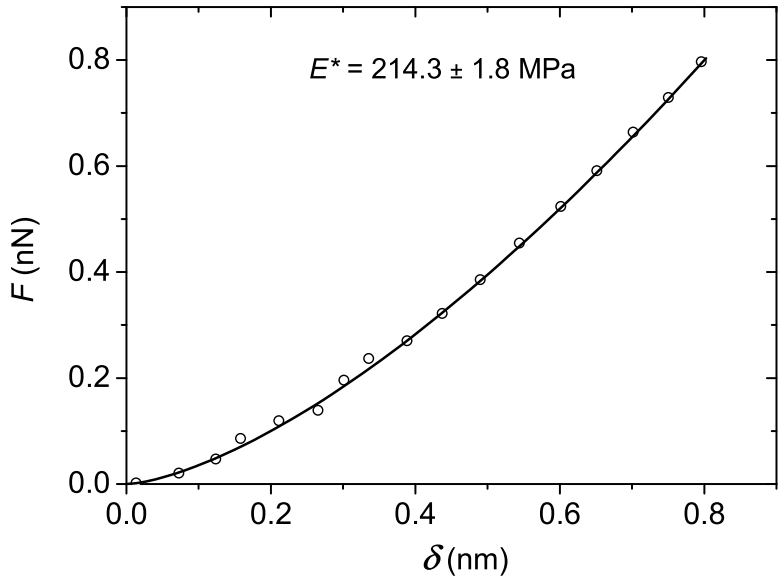

(b)

Figure 4.3: Typical load F versus indentation δ curves obtained for (a) PyTp film, and (b) PyTp-DNA complex film. The curves were fitted with the Hertz model (solid lines), yielding reduced elastic modulus E^* value of 77.1 ± 1.3 MPa for the pure film and 214.3 ± 1.8 MPa for the complex film.

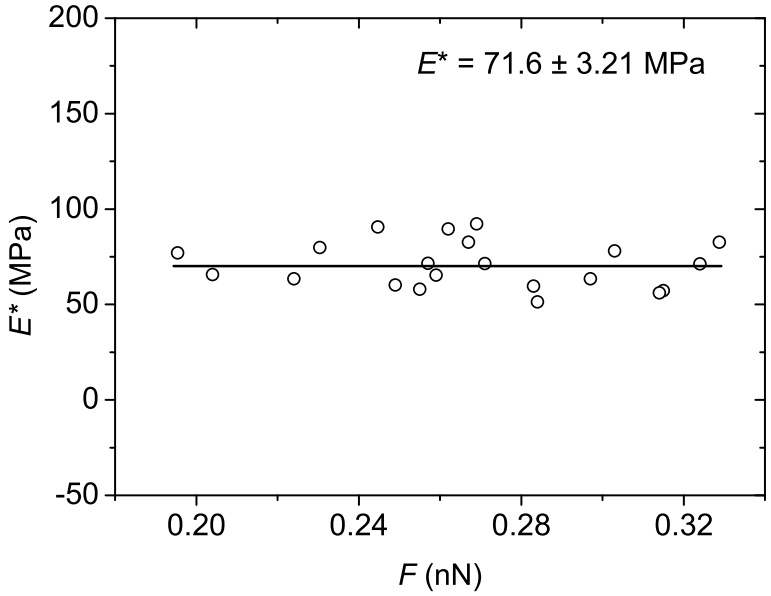

(a)

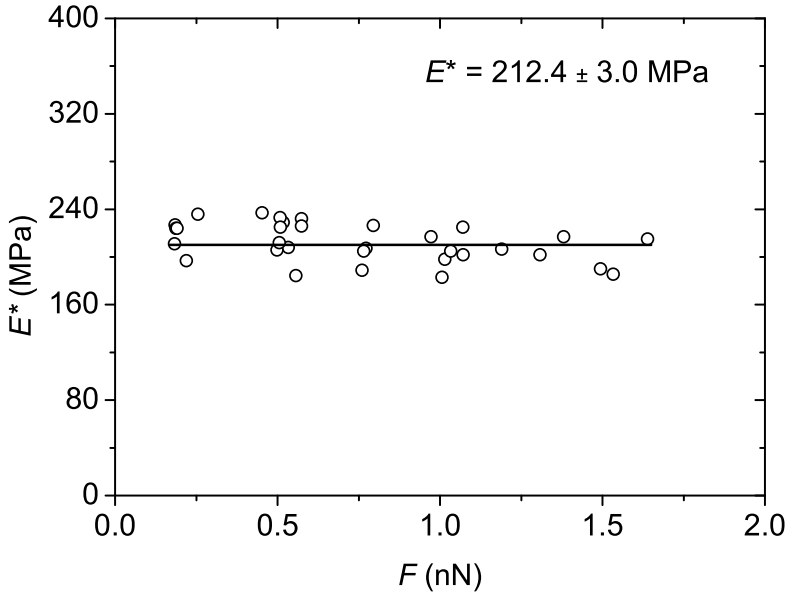

(b)

Figure 4.4: Reduced elastic modulus E^* values plotted for different loads: (a) PyTp film, and (b) PyTp-DNA complex film. These E^* values were calculated from the F versus δ curves acquired at different positions on the film surfaces under different loads.

elastic modulus, E to be 53.7 ± 2.4 MPa and 159.3 ± 2.3 MPa for the pure PyTp and PyTp-DNA complex film surfaces respectively.

4.4.2 Topography and Phase Images using AFM in the Tapping Mode

Figures 4.5(a) and 4.5(b) show simultaneously acquired topography and phase images for PyTp film with two layers on hydrophobic silicon substrate. The topography revealed a smooth and uniform film surface. The phase image exhibited negligible variation in the values of phase shifts on the film. Figure 4.5(c) shows the height and phase shift profiles corresponding to the lines drawn on the topography and phase images, respectively. We have deliberately selected a region which is partially covered with film so that the difference in phase shift between the film surface and the exposed silicon substrate can be revealed. The film height is 4.5 nm as shown by the height profile. The phase shift is greater on the film surface than on the exposed silicon substrate by 2^0. The spikes in the phase profile at the edges of the film surface (Figure 4.5(c)) are due to topographic effects which arise due to the finite feedback response time.

Figures 4.6(a) and 4.6(b) show the topography and phase images of LB film of PyTp-DNA complex with single layer on hydrophilic silicon substrate. The height and phase shift profiles for the lines drawn on the corresponding images are shown in Figure 4.6(c). The topography reveals a compact film surface. The Fourier transform of the phase image (inset in Figure 4.6(b)) reveals a 2-fold symmetry. In addition, the autocorrelation image (Figure 4.7(a)) constructed from this phase image clearly shows a periodic structure. From the profile (Figure 4.7(b)) corresponding to the line drawn across the peaks in the autocorrelation image, the periodicity is calculated to be 36 nm.

4.4.3 Energy Dissipation Maps Constructed from the AFM Phase Images

The energy dissipation map provides qualitative insight of the mechanical properties of a film surface. The energy dissipation map constructed from the phase image of the pure PyTp film with 2 layers is shown in Figure 4.8. Similar maps for the PyTp-DNA complex films with 1 and 5

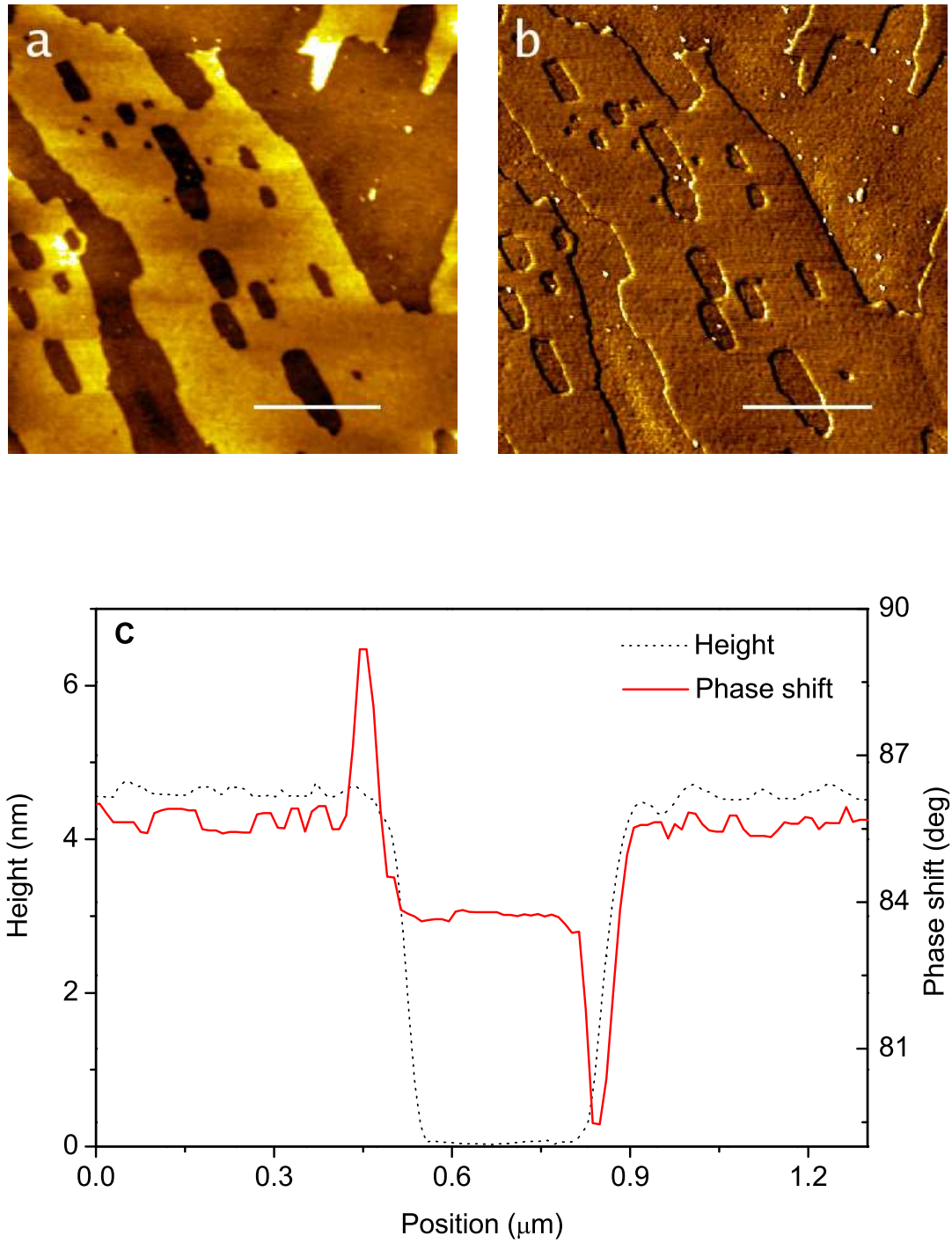

Figure 4.5: Tapping mode AFM images of the PyTp LB film with two layers; (a) topography image, (b) phase image, acquired simultaneously. (c) The height (dotted line) and phase (solid line) profiles corresponding to the lines drawn on the topography and phase images, respectively.

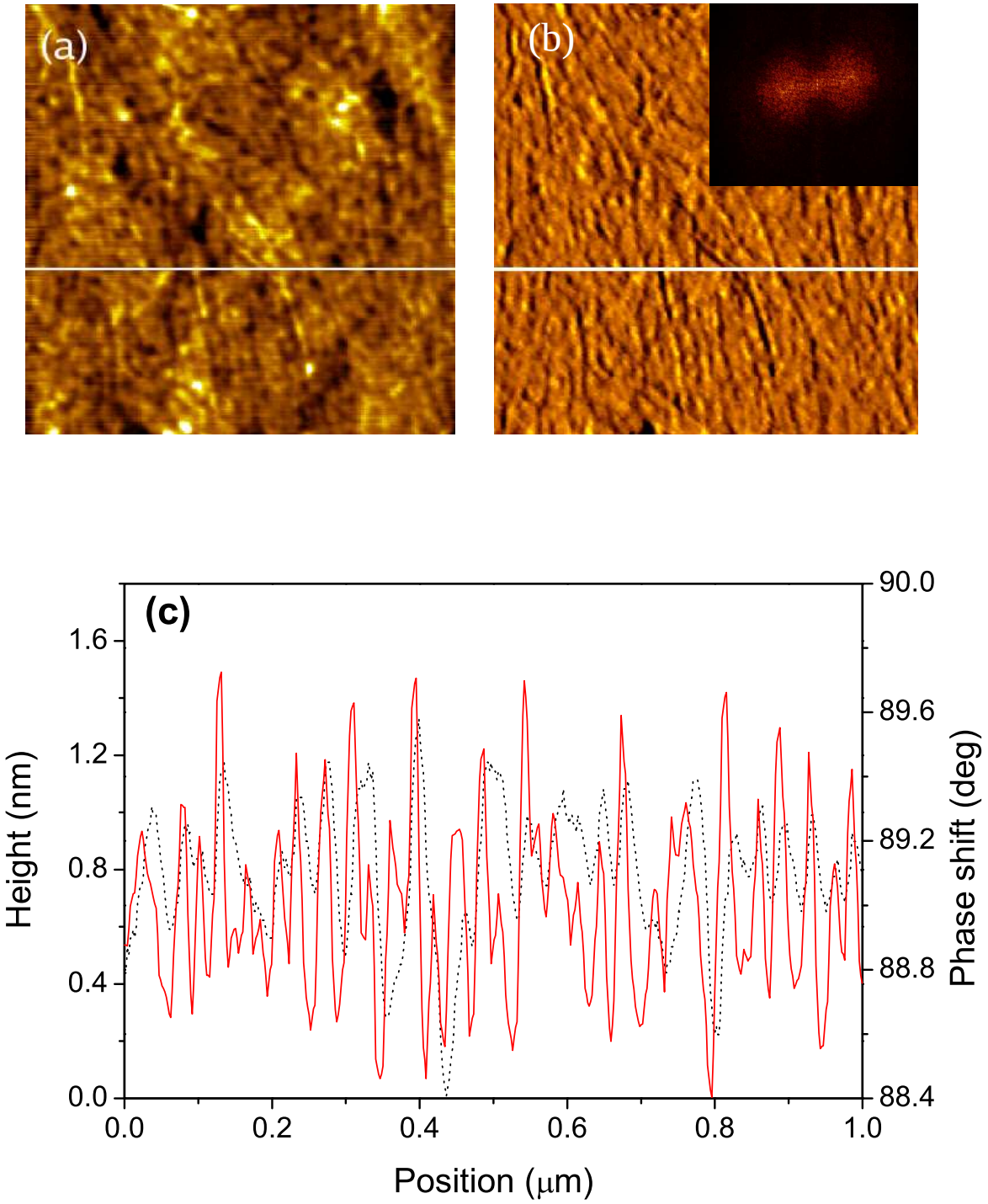

Figure 4.6: Tapping mode AFM images of the PyTp-DNA complex LB film with one layer; (a) topography image, (b) phase image, acquired simultaneously. The Fourier transform of the phase image (inset in (b)) shows a 2-fold symmetry. (c) The height (dotted line) and phase (solid line) profiles corresponding to the lines drawn on the topography and phase images, respectively.

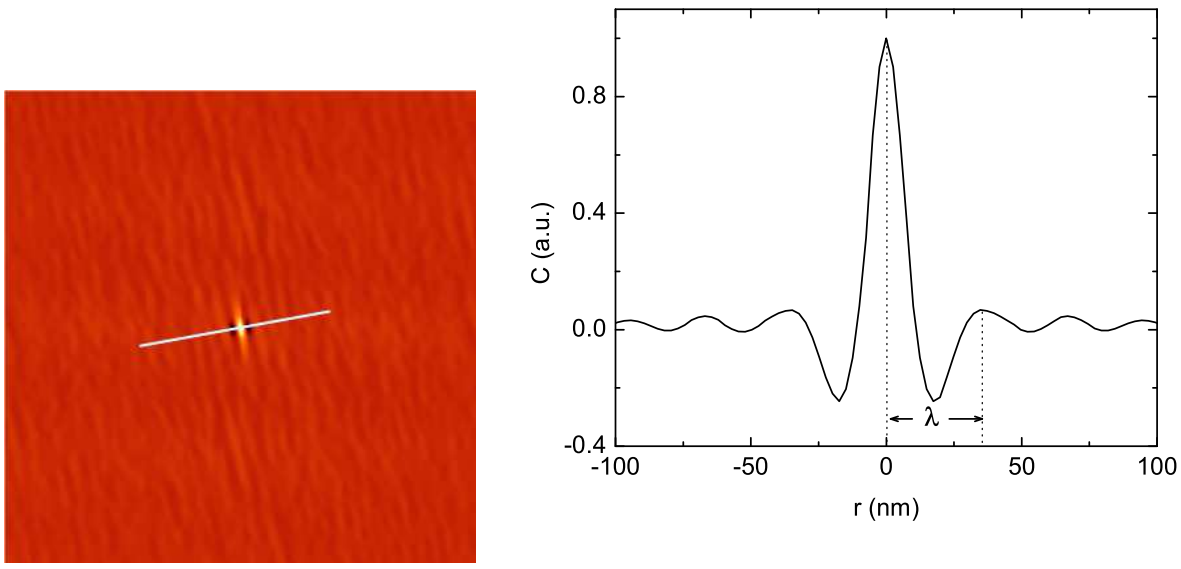

(a) (b)

Figure 4.7: (a) Autocorrelation image of Figure 4.6(b). (b) The profile corresponding to the line drawn across the peaks on the autocorrelation image gives a periodicity (λ) of 36 nm.

layers constructed from the respective phase images are shown in Figures 4.9(a) and 4.9(b). For 20 layers of the complex film, we have shown the topography, phase image and energy dissipation map in Figure 4.10. The average values of energy dissipation (E_{dis}) calculated from these maps and the variation in energy dissipation (ΔE_{dis}) values are presented in Table 4.1. It can be seen that, for the pure film, the average value of E_{dis} was higher compared to that for the complex films. For the complex films, the ΔE_{dis} values increase with increasing number of layers. Also, they are high compared to the pure film. In addition, similar calculations for LB films with different layers of the pure film show that ΔE_{dis} value is small and remains almost the same with increasing number of layers. For the complex film with 20 layers, the topography image (Figure 4.10(a)) shows well aligned DNA bundles. The phase image (Figure 4.10(b)) shows a phase shift variation of about 16^0. The energy dissipation map (Figure 4.10(c)) shows comparatively less E_{dis} values at the regions of DNA bundles.

LB film	No. of layers	Average E_{dis} (eV)	ΔE_{dis} (eV)
Pure	2	1565	8
Complex	1	974	16
Complex	5	711	74
Complex	20	462	109

Table 4.1: The energy dissipation values obtained from the phase shift data of pure PyTp and PyTp-DNA complex LB films.

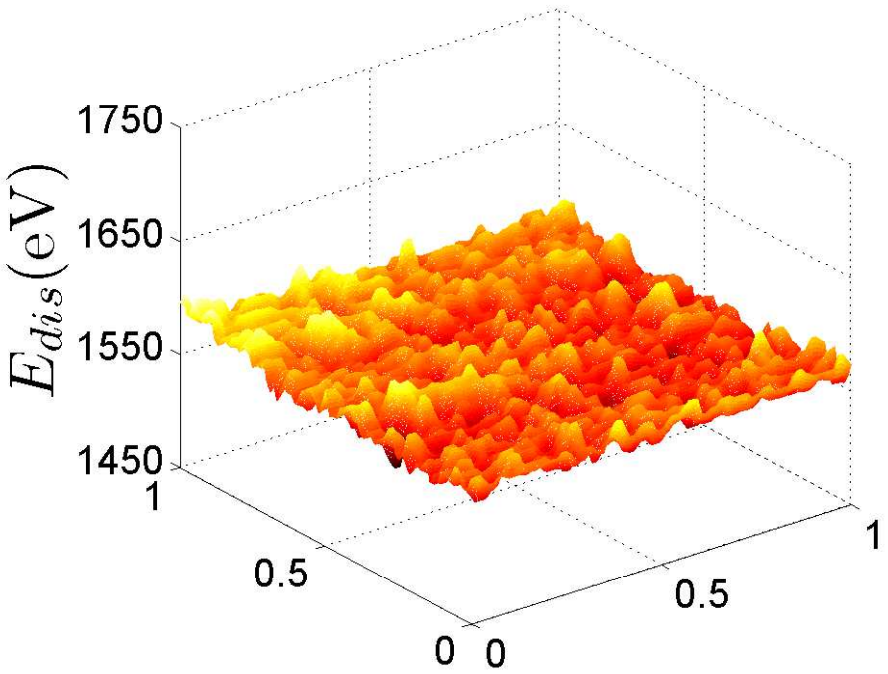

Figure 4.8: The energy dissipation (E_{dis}) map for the pure PyTp LB film with 2 layers constructed for a scan range of 1 × 1 μm^2. Tapping mode data: f_0 = 162.8 kHz, f = 162.5 kHz, A_0 = 54 nm, A_{sp} = 35 nm and Q = 125. Figure was constructed using MATLAB software.

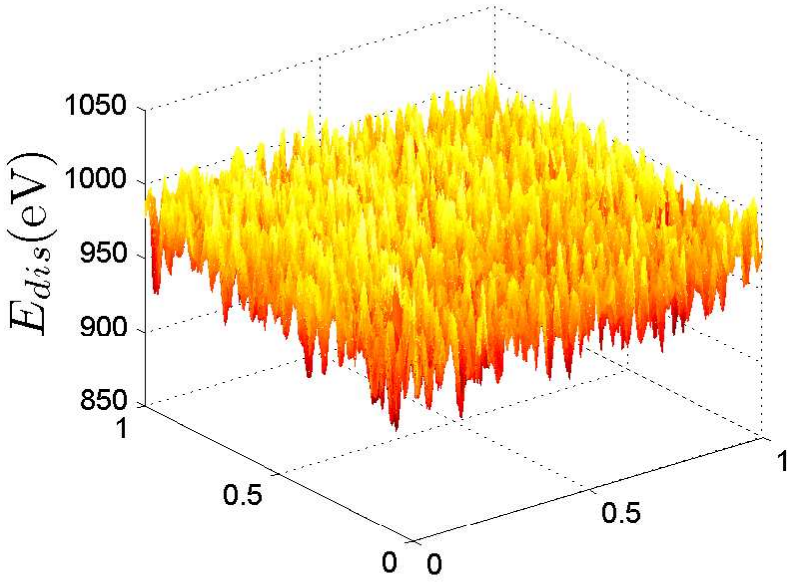

(a)

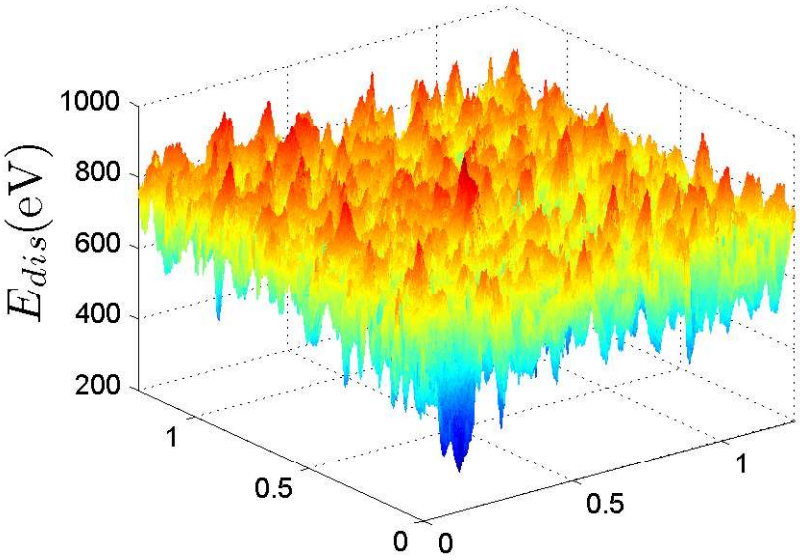

(b)

Figure 4.9: (a) The energy dissipation (E_{dis}) map for the PyTp-DNA complex LB film with 1 layer with a scan range of 1 × 1 μm^2. Tapping mode data: f_0 = 162.95 kHz, f = 162.75 kHz, A_0 = 43 nm, A_{sp} = 31 nm and Q = 181. (b) The E_{dis} map for the PyTp-DNA complex LB film with 5 layers with a scan range of 1.25 × 1.25 μm^2. Tapping mode data: f_0 = 162.94 kHz, f = 162.73 kHz, A_0 = 42.4 nm, A_{sp} = 31.2 nm and Q = 179.7. Figures (a) and (b) were constructed using MATLAB software.

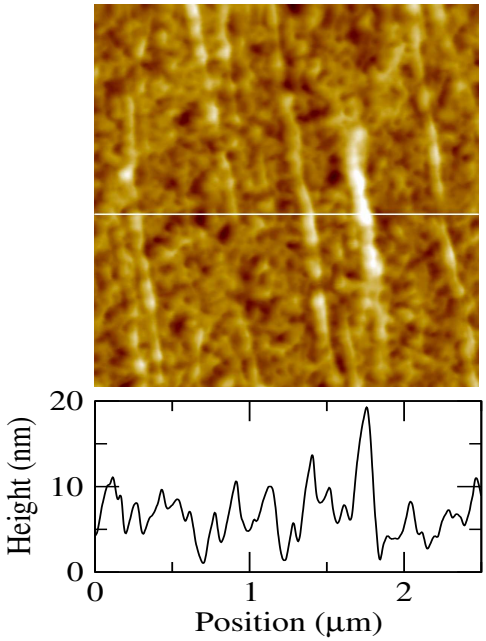

(a)

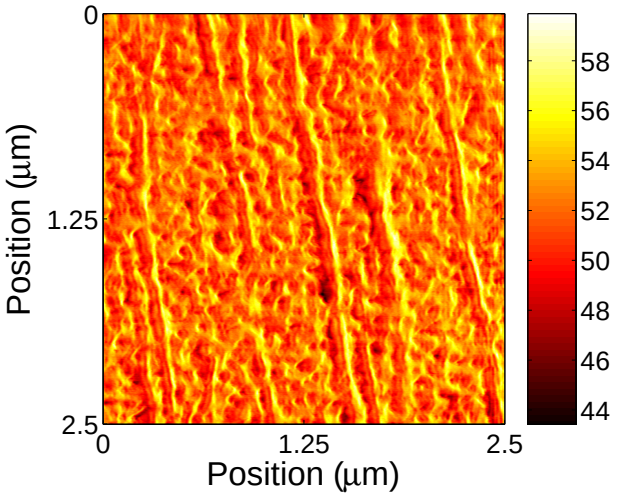

(b)

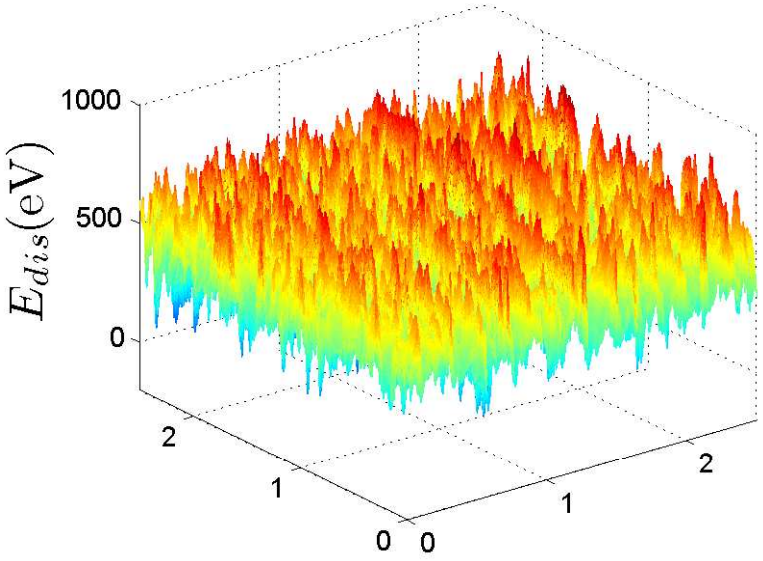

(c)

Figure 4.10: Tapping mode AFM images of the PyTp-DNA complex LB film with 20 layers: (a) Topography image, showing height profile. (b) Simultaneously acquired phase image, the scale bar shows phase shift in degrees. (c) The energy dissipation (E_{dis}) map constructed from the phase image. Tapping mode data: f_0 = 162.95 kHz, f = 162.75 kHz, A_0 = 40 nm, A_{sp} = 30 nm and Q = 183. Figures (b) and (c) were constructed using MATLAB software.

4.5 Discussion

In the previous chapter, we have estimated the hardness of the film surfaces under plastic deformation. We have shown that the PyTp-DNA complex film is two times harder than the pure PyTp film. However, hardness is a *qualitative measurement* which has a considerable error bar (±25%). This is due to two reasons; firstly, the indent formed by the tip on the film surface is generally not uniform. This makes it difficult to measure the area accurately. Secondly, we are imaging the indent with the same tip that was used for indentation which may result in imaging artifacts. Therefore, we can only comment qualitatively on the relative hardness values [22, 30]. In this chapter, we have presented the *quantitative analysis* of the cantilever deflection (d) versus piezo displacement (z) curves obtained for elastic deformation of the film surfaces. We have used Hertz contact mechanics model for the analysis and determined the Young's elastic modulus (E) of the films.

In the cantilever deflection versus piezo displacement curves (Figures 4.2(a) and 4.2(b)), the slope is 1 for the reference silicon surface because silicon is an infinitely stiff surface compared to the cantilever stiffness. On the other hand, when the tip indents the film surface, the cantilever deflection becomes smaller than the piezo vertical displacement. This results in a slope smaller than 1. From the load (F) versus indentation (δ) curves (Figures 4.3(a) and 4.3(b)), it can be seen that for a given load, the depth of indentation was more on the pure film than on the complex film indicating the pure film to be softer than the complex film. This is in accordance with the hardness (plastic deformation) measurements of these films described in Chapter 3. Here, we are interested in measuring the elastic modulus of the film surfaces quantitatively. Therefore, we have carried out indentation precisely under small load ($\sim$ 1 nN) to avoid any plastic deformation. The film surface was imaged before and after indentation to ensure that the deformation was elastic. Hertz model is valid for elastic deformations and does not take into account tip-sample adhesion. Since adhesion forces were negligible in this study (using dry nitrogen gas atmosphere) and the deformation was elastic, it was reasonable to use this model. It was observed that the F versus δ curves for both the films fit well with the paraboloid model. Hence, we have fitted all the F versus δ curves with paraboloid model to calculate the Young's modulus values. We have repeated the measurements

several times for different loads and at different positions on the films (Figures 4.4(a) and 4.4(b)). From all these measurements, we find that the Young's modulus value is 53.7 MPa for the pure film and 159.3 MPa for the complex film. This indicates that the complex film is about 3 times stiffer than the pure film, since the elastic modulus of a film is directly related to its stiffness (equation 4.16). The elastic modulus of films are important in surface mechanical properties of materials and in understanding the role of interface in defect production [31].

The phase imaging in tapping mode AFM is known to be a powerful method for mapping the variations in composition, viscoelasticity, stiffness and adhesion of the sample surface at high spatial resolution. However, the phenomenon affecting the contrast in a phase image is complex. The changes in phase shift during scanning depends on several factors like tip-sample separation, deformation at the tip-sample contact, interaction regime, cantilever properties (spring constant, quality factor), tip geometry and the level of tapping force [16]. Also, the phase shift can be affected by changes in topographic features. Therefore, extracting information contained in a phase image should be done carefully.

For correct interpretation of phase images, the level of tapping force must be taken into account. The level of tapping force used during imaging is related to the set-point ratio (r_{sp}) which is defined as the ratio of set-point amplitude (A_{sp}) to free-oscillation amplitude (A_0). The force levels corresponding to a r_{sp} of 0.9-0.8 is light tapping (attractive regime) and 0.8-0.4 is hard tapping (repulsive regime) [32]. The phase shift can be dominated by the tip-sample contact area. In light tapping, the hard and soft parts show similar phase shifts close to zero because the tip-sample contact is minimal. Here, the probe response is not dominated by the tip-sample repulsive force but is strongly influenced by surface attractive forces such as capillary force and adhesion. In addition, the phase imaging with light tapping may record only the changes in the gradient of the topography [33]. On the other hand, for hard tapping, phase shift of the softer part becomes larger than that of the harder part, because the contact area becomes much larger on the softer part. Here, the probe response is dominated by the tip-sample repulsive interaction. Imaging at hard tapping is known to be best suited for mapping stiffness variations on sample surfaces [26]. We have performed phase imaging at hard tapping. Therefore, in all our phase images, the soft

region appears brighter (more phase shift) compared to the hard region. For the PyTp film (Figure 4.5(b)), the phase shift was found to be greater on the film surface by 2^0 than on the exposed silicon substrate indicating the film surface to be softer. We would like to mention that the phase image exhibited comparatively less contrast since both the PyTp film surface as well as the exposed silicon substrate were hydrophobic [34]. Additionally, phase imaging can give information about the organization of molecules on a surface. In literature, phase images of LB films of some single component systems (e.g., fatty acids, cholesterol) have been reported to reveal regions of different polarity due to the flipping of the constituent molecules [35, 36]. In our system, the phase image of PyTp LB film (Figure 4.5(b)) showed negligible variation in phase shifts suggesting uniform polarity of the film surface. This may be due to the fact that the strong π-π interaction between the adjacent discotic cores inhibit flipping of constituent molecules in the film.

Phase imaging is known to improve the resolution and contrast of images as compared with the topography image [33]. For the LB film of PyTp-DNA complex on hydrophilic silicon substrate, the phase image (Figure 4.6(b)) revealed a periodic structure which was not clearly resolved in the topography image. We have performed autocorrelation of the image to find the periodicity [37]. Autocorrelation is defined as, $G(k1, k2) = \Sigma f(x, y) f(x + k1, y + k2)$ where f(x,y) is the image matrix. This equation takes the image and the same image shifted at a distance k1 and k2 in the X and Y-axis with respect to the center of the image. The more similar the image and the shifted image are, the higher the value of the autocorrelation. The highest value in autocorrelation is obtained at the center of the image (where k1 and k2 are zero). Any periodicity in the original image will be shown as a periodic pattern in the autocorrelation. We have obtained a periodicity of 36 nm from the autocorrelation of the phase image of PyTp-DNA complex film (Figure 4.7(b)). This value is much greater than the diameter of a DNA double strand (~2 nm) suggesting these to be DNA bundles. The strong π-π stacking interaction between the discotic cores brings multiple DNA strands together forming bundles. Additionally, the alignment of these DNA bundles in the periodic structure was observed predominantly in the film deposition direction. In literature, this has been attributed to the possibility that when a substrate is withdrawn from the subphase in the process of LB film deposition, the receding meniscus force tries to align the DNA strands parallel

to its direction [38, 39].

The nanoindentation technique using an AFM gives *local* elastic modulus [40]. For a qualitative understanding of the variation in elastic properties over a sample surface, the phase imaging in the tapping mode AFM is very useful. Magonov et al. have shown that the phase shift arising from the damping in the tip oscillation due to the tip-sample interactions can be related to the surface stiffness [26]. It is to be noted that the phase shift data depends on the interaction regime. This renders direct phase shift measurements less useful to map material properties. Therefore, it is more convenient to transform phase shift data into energy dissipation values by means of equation 4.19 to map the variations in material properties like stiffness [16]. From the energy dissipation maps (Figure 4.8 and Figure 4.9), we find that the PyTp film exhibited higher E_{dis} value as compared to the PyTp-DNA complex films. This may be attributed to the larger damping in tip oscillation for the pure film due to its soft nature which leads to a larger energy dissipation. This result confirms the nanoindentation result that showed the pure film to be soft as compared with the complex film. In addition, we find that, for the complex films, the ΔE_{dis} values increase with increasing number of layers, whereas, for the pure films, it remains almost the same with increasing number of layers. This suggests that unlike complex film, the surface stiffness of the pure film remains uniform irrespective of the number of layers. This may be attributed to the fact that the pure film is composed of well packed discotic molecules due to the strong π-π interaction between the cores. This leads to a uniform film surface with the molecules arranged in a two-dimensional columnar structure on the substrate [41]. For the complex film, such an ordering may not be possible due to the presence of DNA. The non-uniformity in the surface stiffness for the complex film can be clearly seen from the energy dissipation map for 20 layers (Figure 4.10(c)) which shows comparatively less E_{dis} values at the regions of DNA bundles indicating these regions to be stiffer. Thus, with the help of phase imaging, we could continuously map the variation in elastic properties over the film surfaces.

On the basis of these results and the results from nanoindentation measurements, we suggest that the pure film is soft and comparatively uniform, whereas for the complex film, the surface is stiff and becomes more and more non-uniform with increasing number of layers. Nanoindentation measurements can give elastic modulus values only at a point, whereas the phase imaging

provides continuous maps of variation in stiffness over a sample surface. Hence, the nanoindentation technique, when used together with phase imaging, provides a better understanding of the mechanical properties of film surfaces. The PyTp and PyTp-DNA complex films have potential for applications in devices like field-effect transistors and biosensors [4, 42]. Therefore, the mechanical property studies of such films at nanoscale are of importance in the design and development of nanodevices.

4.6 Conclusions

We have studied the nanoscale mechanical properties of LB films of the pure PyTp as well as the PyTp-DNA complex using an AFM. From the nanoindentation measurements, we have calculated the Young's elastic modulus values to be 54 and 160 MPa for the pure and complex films respectively. In addition, phase shift measurements were carried out for these films and energy dissipation maps were constructed. The phase image for the LB film of PyTp-DNA complex with single layer clearly resolved a periodic structure. The qualitative analysis of the energy dissipation maps showed that the surface of the pure film is soft and uniform, whereas, the complex film surface is stiff and non-uniform. Nanoindentation measurements gave local elastic modulus of the film surfaces, whereas with the help of phase imaging, we could continuously map the variation in elastic properties over the film surfaces.

Discogens are considered as a new generation of organic semiconductors. They possess unique molecular electronic features, like the two-dimensional delocalization of electrons, that are not observed in linear oligomers and polymers. The known examples of successfully operating electronic devices based on discotic semiconductors are field-effect transistors, photovoltaic solar cells and light-emitting diodes. Therefore, the electrical property measurements of the films of discogens are of prime interest. In the next chapter, we investigate the electrical properties of pure PyTp film and PyTp-DNA complex film using a special mode of AFM, i.e., the current-sensing AFM.

Bibliography

[1] J. O. Radler, I. Koltover, T. Salditt, and C. R. Safinya, *Science* **275**, 810 (1997).

[2] D. Putnam, *Nature Materials* **5**, 439 (2006).

[3] H. Nakayama, H. Ohno, and Y. Okahata, *Chem. Commun.*, 2300 (2001).

[4] G. B. Sukhorukov, M. M. Montrel, A. I. Petrov, L. I. Shabarchina, and B. I. Sukhorukov, *Biosensors and Bioelectronics* **11**, 913 (1996).

[5] T. Fukushima, T. Hayakawa, Y. Inoue, K. Miyazaki, and Y. Okahata, *Biomaterials* **25**, 5491 (2004).

[6] L. Wang, J. Yoshida, N. Ogata, S. Sasaki, and T. Kajiyama, *Chem. Mater.* **13**, 1273 (2001).

[7] L. Cui, J. Miao, and L. Zhu, *Macromolecules* **39**, 2536 (2006).

[8] Alpana Nayak and K. A. Suresh, *J. Phys. Chem. B* **112**, 2930 (2008).

[9] D. K. Schwartz, *Surface Science Reports* **27**, 241 (1997).

[10] E. W. Wong, P. E. Sheehan, and C. M. Lieber, *Science* **277**, 1971 (1997).

[11] M. Radmacher, M. Fritz, and P. K. Hansma, *Biophysical Journal* **69**, 264 (1995).

[12] A. Touhami, B. Nysten, and Y. F. Dufrene, *Langmuir* **19**, 4539 (2003).

[13] M. S. Marcus, R. W. Carpick, D. Y. Sasaki, and M. A. Eriksson, *Phys. Rev. Lett.* **88**, 226103 (2002).

[14] D. Raghavan, X. Gu, T. Nguyen, M. VanLandingham, and A. Karim, *Macromolecules* **33**, 2573 (2000).

[15] B. Cappella and G. Dietler, *Surface Science Reports* **34**, 1 (1999).

[16] N. F. Martinez and R. Garcia, *Nanotechnology* **17**, S167 (2006).

[17] N. A. Burnham, X. Chen, C. S. Hodges, G. A. Matei, E. J. Thoreson, C. J. Roberts, M. C. Davies, and S. J. B. Tendler, *Nanotechnology* **14**, 1 (2003).

[18] J. L. Hutter and J. Bechhoefer, *Rev. Sci. Instrum.* **64** (7), 1868 (1993).

[19] H. Hertz, *J. Reine Angew. Math.* **92**, 156 (1882).

[20] S. Tan, R. L. Sherman Jr., and W. T. Ford, *Langmuir* **20**, 7015 (2004).

[21] R. P. Feynman, R. Leighton, and M. Sands, *The Feynman lectures on Physics*, Addison-Wesley Publishing Co.: Vol. 2, Chapter 38, p 1311.

[22] D. H. Gracias and G. A. Somorjai, *Macromolecules* **31**, 1269 (1998).

[23] R. Garcia and A. S. Paulo, *Phys. Rev. B* **60**, 4961 (1999).

[24] U. Rabe, J. Turner, and W. Arnold, *Appl. Phys. A: Mater. Sci. Process.* **66**, S277 (1998).

[25] G. Chen, R. Warmack, A. Huang, and T. Thundat, *J. Appl. Phys.* **78**, 1465 (1995).

[26] S. N. Magonov, V. Elings, and M. H. Whangbo, *Surf. Sci.* **375**, L385 (1997).

[27] G. Haugstad and R. R. Jones, *Ultramicroscopy* **76**, 77 (1999).

[28] J. P. Cleveland, B. Anczykowski, A. E. Schmid, and V. Elings, *Appl. Phys. Lett.* **72**, 2613 (1998).

[29] J. Tamayo and R. Garcia, *Appl. Phys. Lett.* **73**, 2926 (1998).

[30] B. Bhushan, A. V. Kulkarni, V. N. Koinkar, M. Boehm, L. Odoni, C. Martelet, and M. Belin, *Langmuir* **11**, 3189 (1995).

[31] R. C. Thomas, J. E. Houston, T. A. Michalske, and R. M. Crooks, *Science* **259**, 1883 (1993).

[32] M. Lemieux, D. Usov, S. Minko, M. Stamm, H. Shulha, and V. V. Tsukruk, *Macromolecules* **36**, 7244 (2003).

[33] X. Chen, S. L. McGurk, M. C. Davies, C. J. Roberts, K. M. Shakesheff, S. J. B. Tendler, P. M. Williams, J. Davies, A. C. Dawkes, and A. Domb, *Macromolecules* **31**, 2278 (1998).

[34] J. I. Paredes, A. Martinez-Alonso, and J. M. D. Tascon, *Langmuir* **18**, 4314 (2002).

[35] D. Y. Takamoto, E. Aydil, J. A. Zasadzinski, A. T. Ivanova, D. K. Schwartz, T. Yang, and P. S. Cremer, *Science* **293**, 1292 (2001).

[36] Raj Kumar Gupta and K. A. Suresh, *Eur. Phys. J. E* **14**, 35 (2004).

[37] J. C. Russ, *The Image Processing Handbook* : CRC Press **2002** Fourth Edition, page 331, chapter 5.

[38] Y. Okahata, T. Kobayashi, and K. Tanaka, *Langmuir* **12**, 1326 (1996).

[39] A. Bhaumik, M. Ramakanth, L. K. Brar, A. K. Raychaudhuri, F. Rondelez, and D. Chatterji, *Langmuir* **20**, 5891 (2004).

[40] D. DeVecchio and B. Bhushan, *Rev. Sci. Instrum.* **68**, 4498 (1997).

[41] N. C. Maliszewskyj, P. A. Heiney, J. Y. Josefowicz, J. P. McCauley, and A. B. Smith, *Science* **264**, 77 (1994).

[42] S. Sergeyev, W. Pisula, and Y. H. Geerts, *Chem. Soc. Rev.* **36**, 1902 (2007).